

Enhanced Hemispheric Thermal Contrast Intensified the Indian Monsoon During the Last Interglacial

Kaiqi Chen¹, Qiong Zhang², Josefine Axelsson², Jianping Li³, and Lanning Wang⁴

¹

²Stockholm University

³Frontiers Science Center for Deep Ocean Multispheres and Earth System (FDOMES)

⁴Beijing Normal University

November 24, 2022

Abstract

Observational data from the past century show a weakening trend in summer monsoon over the Indian subcontinent. This is possibly attributed to the reduced land–sea contrast resulting from the Indian Ocean warming under the rapid increase of greenhouse gases in the atmosphere. In contrast, speleothem records indicate that the Indian summer monsoon was stronger during the last interglacial (LIG) warm period than it is today. Using climate model simulations, we show that orbital forcing effect during the LIG, as well as related ocean feedbacks, led to warming in the Eurasian continent and cooling in the Indian Ocean basin. This amplified the land–sea contrast in the region and intensified the Indian summer monsoon. Although the LIG is often portrayed as a potential analogue of future climate, our study shows that the Indian monsoon responded differently to the LIG warming period than it does to current climate warming.

24 **Abstract**

25 Observational data from the past century show a weakening trend in summer monsoon over the
26 Indian subcontinent. This is possibly attributed to the reduced land–sea contrast resulting from
27 the Indian Ocean warming under the rapid increase of greenhouse gases in the atmosphere. In
28 contrast, speleothem records indicate that the Indian summer monsoon was stronger during the
29 last interglacial (LIG) warm period than it is today. Using climate model simulations, we show
30 that orbital forcing effect during the LIG, as well as related ocean feedbacks, led to warming in
31 the Eurasian continent and cooling in the Indian Ocean basin. This amplified the land–sea
32 contrast in the region and intensified the Indian summer monsoon. Although the LIG is often
33 portrayed as a potential analogue of future climate, our study shows that the Indian monsoon
34 responded differently to the LIG warming period than it does to current climate warming.

35 **Plain Language Summary**

36 One way to understand the future climate changes is to learn from the past warm periods. In this
37 case the Last Interglacial (LIG) is often referred as a potential analogue. However, the
38 paleoclimate proxy data such as the speleothem records show a stronger Indian summer
39 monsoon (ISM) in the LIG, in contrast to an observed weakening trend in ISM in past century. In
40 this study we use the climate model simulations to explain why the opposite changes happened
41 in ISM during LIG and current global warming. The warming in the LIG was caused by changed
42 distribution of solar radiation over the earth, which is different to the current warming resulted
43 from increased Greenhouse Gas concentration in the atmosphere. The changes in Indian
44 monsoon are mainly determined by the land-sea contrast in the region. Due to its special
45 geographical location, i.e., north-south orientations of land-sea distribution, the solar radiation
46 changes in LIG enhanced the land-sea contrast and thus intensified the summer monsoon. We
47 suggest that although the LIG is often portrayed as a potential analogue for future climate
48 change, the analogy does not hold in the Indian monsoon region.

49 **1 Introduction**

50 As one of the most powerful tropical monsoon climate systems in the world, the Indian summer
51 monsoon (ISM) can bring moisture from the Indian Ocean towards the continent, resulting in
52 heavy precipitation (Buckley et al., 2014). Even small changes in precipitation over the Indian
53 subcontinent could have significant consequences for agricultural production and socio-
54 economic development (Gadgil & Kumar, 2006; Singh et al., 2014; Vittal et al., 2020). Previous
55 studies have shown that changes to the ISM are highly sensitive to global warming (Kitoh et al.,
56 2013). The frequency of moderate precipitation events and the strength of summer monsoon over
57 the Indian subcontinent have exhibited a significant weakening trend over the past century
58 (Goswami et al., 2006; Li & Zeng, 2002). Meanwhile, global warming has caused sea surface
59 temperature (SST) in the tropical eastern Indian Ocean to rise, which has resulted in a weakening
60 of the land–sea thermal gradient and reduced Indian summer monsoon precipitation (Dinezio et
61 al., 2020; Ramesh & Goswami, 2007; Roxy et al., 2015). Climate models participating in the
62 fifth Climate Model Intercomparison Project (CMIP5) show a large uncertainty in their
63 projections of the Indian monsoon system (Saha et al., 2014). It has been suggested that past
64 warm climates could be used as a potential analogue to understand future climate changes. As
65 part of CMIP, the Paleoclimate Model Intercomparison Project (PMIP) aims to evaluate the
66 ability of CMIP6 models to reproduce past climate by comparing with paleoclimate proxy-data

67 records and to further our understanding of regional responses to a warmer climate, such as
68 changes in the Indian monsoon (Harrison et al., 2015; Hirabayashi et al., 2013).

69 The most recent warm period is the last interglacial (LIG), which lasted from 129 to 116
70 thousand years (ka) before present. During the LIG, the geographical setting and concentration
71 of greenhouse gases (GHGs) in the atmosphere were almost the same as in the present day. The
72 main difference was the incoming solar radiation caused by changes in the Earth's orbit. The
73 global mean surface air temperature was ~ 2 °C higher than in the CMIP6 piControl for 1850 CE
74 (PI) (Hoffman et al., 2017; Turney et al., 2020), and surface temperatures in the northern middle
75 and high latitudes were about 2–5 °C higher (Turney & Jones, 2010). These global and
76 hemispheric warming features are similar to projections of future global warming (Otto-Bliesner
77 et al., 2017). The signal of long-term precipitation changes in the Indian monsoon have been
78 mostly recorded in marine sediments and cave deposits (Cai et al., 2015; Cheng et al., 2016;
79 Midhun et al., 2018). The $\delta^{18}\text{O}$ signal recorded in stalagmites is one of the most important water
80 tracers, but it has given conflicting results regarding changes in Asian monsoon precipitation.
81 Previous studies have combined stalagmite $\delta^{18}\text{O}$, $\delta^{44}\text{Ca}$, and elemental ratios (e.g., Mg/Ca, Sr/Ca,
82 and Ba/Ca) and shown that the ISM was unstable during the LIG (Magiera et al., 2019). Some
83 other proxy records also showed varied changes in the Asian monsoon (Wang et al., 2008). One
84 reason for this is that the variation in $\delta^{18}\text{O}$ is affected by large-scale atmospheric dynamics more
85 than by regional precipitation (Li, 2018; Tan, 2014).

86 The LIG has been one of the main target periods in PMIP since PMIP3 (Masa et al., 2018).
87 Multiple model ensembles show that there is a significant warming in almost all continents
88 during boreal summer (Lunt et al., 2013; Nikolova et al., 2013; Pedersen et al., 2017). The
89 increased Indian summer monsoon precipitation observed during the LIG contrasts with the
90 decreased Indian summer monsoon precipitation projected under continuous global warming
91 (Turner & Annamalai, 2012). Scussolini et al.(2019) note that the significant increase of Indian
92 summer monsoon precipitation during the LIG period is consistent with the increase of cloud
93 cover and surface cooling. However, there is still a large gap in our understanding of the
94 dynamics of Indian summer monsoon precipitation during the LIG period compared with the
95 Holocene and the present (Han et al., 2019; Lechleitner et al., 2017; Sinha et al., 2015). Current
96 global warming has provided an important impetus to study climatology at higher global
97 temperatures. Understanding the dynamics of ISM precipitation during the LIG will also provide
98 a strong scientific basis for predicting spatiotemporal changes in the Indian climate.

99 Here we use simulations from the global coupled climate model EC-Earth3 and analyze climatic
100 changes in the ISM region by comparing with a PI control experiment. We find that due to the
101 effect of orbital forcing, Indian summer monsoon precipitation during the LIG increased
102 significantly over the west coast of the Western Ghats and the southern Higher Himalayas but
103 decreased over the equatorial eastern Indian Ocean. These changes in Indian summer monsoon
104 precipitation resulted primarily from enhancement of the hemispheric thermal contrast by
105 changes in orbital forcing, which amplified the land–sea contrast. Meanwhile, the thermal
106 imbalance between the Northern and Southern hemispheres led to an SST anomaly in the Pacific
107 Ocean, which influenced the SST in the eastern Indian Ocean through ocean–atmosphere
108 interactions, enhanced the land–sea contrast over the region, and further intensified the ISM
109 precipitation over the Indian continent.

111 2 Model simulations and methods

112 2.1 EC-Earth model and setup

113 In this study, we use the PMIP4/CMIP6 simulations of the last interglacial and preindustrial
 114 period performed by EC-Earth3-LR (Zhang et al., 2021). EC-Earth is a fully coupled Earth
 115 system model that is developed by a European consortium of around 30 research institutions and
 116 is widely used in various studies on climate change (Hazeleger et al., 2010, 2012). The
 117 atmospheric component of EC-Earth3 is the Integrated Forecasting System model (cycle 36r4)
 118 of the European Center for Medium-Range Weather Forecasts (ECMWF), which contains the
 119 land surface Hydrology Tiled ECMWF Scheme for Surface Exchanges over Land (Balsamo et
 120 al., 2009). The ocean model is the Nucleus for European Modeling of the Ocean (NEMO;
 121 Madec, 2008), coupled with the dynamic–thermodynamic sea-ice model Louvain-la-Neuve
 122 version 3 (LIM3; Vancoppenolle et al., 2012). Atmospheric-land and ocean-sea-ice components
 123 are coupled through the Ocean, Atmosphere, Sea Ice, Soil coupler (Craig et al., 2017). The
 124 horizontal resolution of the atmosphere and land is 125 km with 62 vertical layers in the
 125 atmosphere; the ocean model, NEMO, has a horizontal resolution of 110 km with 75 vertical
 126 layers.

127 We have run the lig127k and piControl simulations following the PMIP4/CMIP6 protocol
 128 (Kageyama et al., 2018). The piControl and lig127k have the same boundary conditions expected
 129 for the orbital forcing and GHGs. A detailed description of the piControl and lig127k simulations
 130 with EC-Earth3-LR is given in Zhang et al. (2021). The orbital forcing is calculated internally in
 131 the model. The orbital parameters are set for 1850 CE in the piControl run and for 127 ka before
 132 present in the lig127k run (the present day is set as 1950 CE in the orbital parameter calculation).
 133 The CO₂, CH₄, and N₂O concentrations in the atmosphere are 284.3 ppm, 808.2 ppb, and 283
 134 ppb in the piControl run and 275 ppm, 586 ppb, and 255 ppb in the lig127k run. The lig127k
 135 simulation starts from the PI initial conditions and has a spin-up time of about 200 years. The
 136 simulation is run for 200 years after reaching equilibrium (i.e., when the global mean
 137 temperature trend is less than 0.05 K per century). We use 200 years of data for the analysis.

138 2.2 Statistical methods and indices

139 To investigate changes to the Indian summer monsoon during the LIG, we use a unified
 140 dynamical normalized seasonality (DNS) monsoon index defined by Li & Zeng (2002). This
 141 index represents the intensity of the monsoon based on the wind field rather than precipitation. It
 142 has been shown that this index represents the seasonal cycle and interannual variability of the
 143 monsoon over various areas well, especially in Asia (Wang et al., 2008). The index has also been
 144 adopted by the National Oceanic and Atmospheric Administration ([http://www.cpc.
 145 noaa.gov/products/Global_Monsoons/Asian_Monsoons](http://www.cpc.noaa.gov/products/Global_Monsoons/Asian_Monsoons)).

146 The DNS index is given by

$$\delta_{nm} = \frac{||\bar{\mathbf{V}}_{winter} - \mathbf{V}_{nm}||}{||\bar{\mathbf{V}}||}, \quad (1)$$

$$\bar{\mathbf{V}} = (\bar{\mathbf{V}}_{winter} + \bar{\mathbf{V}}_{summer})/2, \quad (2)$$

147 where $\bar{\mathbf{V}}_{winter}$ and $\bar{\mathbf{V}}_{summer}$ are the climatological winter and summer reference state wind
 148 vectors and \mathbf{V}_{nm} is the wind vector in a given month. Here, January represents winter and July
 149 represents summer. The norm $\|\mathbf{A}\|$ is defined as

$$\|\mathbf{A}\| = (\iint_S |\mathbf{A}|^2 dS)^{1/2}, \quad (3)$$

150 where S denotes the domain of integration. In calculations at a point (i, j) ,

$$\begin{aligned} \|A_{i,j}\| \approx \Delta S [& (|A_{i-1,j}^2| + 4|A_{i,j}^2| + |A_{i+1,j}^2|) \cos \varphi_j^{1/2} \\ & + |A_{i,j-1}^2| \cos \varphi_{j-1} + |A_{i,j+1}^2| \cos \varphi_{j+1}] \end{aligned}, \quad (4)$$

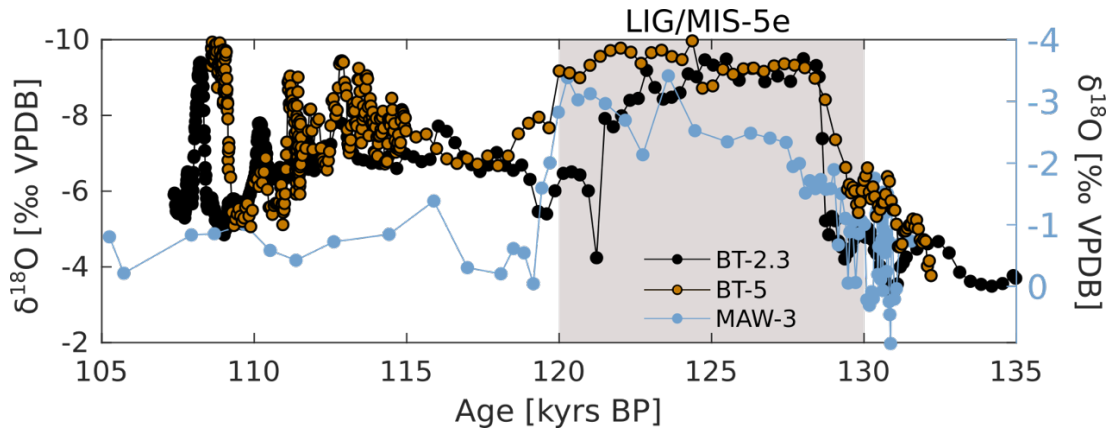
151 where $\Delta S = a\Delta\varphi\Delta\lambda/4$, φ_j is the latitude at the point (i, j) , $\Delta\varphi$ and $\Delta\lambda$ are resolutions in the
 152 meridional and zonal directions, respectively, and a is the mean radius of the Earth (Li & Zeng,
 153 2000).

154 We compute the DNS monsoon index using the monthly mean wind field at 850 hPa from the PI
 155 and LIG simulations.

156

157 **3 Paleo proxy evidence for an intensified Indian summer monsoon during the LIG**

158 Paleo proxy records indicate that South Asia was wetter during the LIG than in the PI period,
 159 mainly because of differences in orbital forcing and higher Northern Hemisphere summer
 160 insolation (Liu et al., 2020; Scussolini et al., 2019). Speleothem records from Bittoo cave
 161 (Khatayat et al., 2016) and Mawmluh cave (Magiera et al., 2019) both show more depleted
 162 oxygen isotopes during Marine Isotope Stage 5e (MIS-5e) than before or after (Fig. 1). Bittoo
 163 cave is situated on the edge of the ISM region in northern India ($30^\circ 47' 25''\text{N}$, $77^\circ 46' 35''\text{E}$) and
 164 receives ~80% of its annual precipitation during the monsoonal months of June–September
 165 (Khatayat et al., 2016). Mawmluh cave is located in northeastern India ($25^\circ 15' 44''\text{N}$,
 166 $91^\circ 52' 54''\text{E}$) and gets 75% of its precipitation during the ISM. The main moisture source for
 167 monsoonal precipitation at both cave sites is the Bay of Bengal. Orographic lifting due to the
 168 Meghalaya Plateau and strong southeasterly flow over central India leads to extreme monsoon
 169 precipitation in this part of the ISM region, especially in northeast India (Magiera et al., 2019).



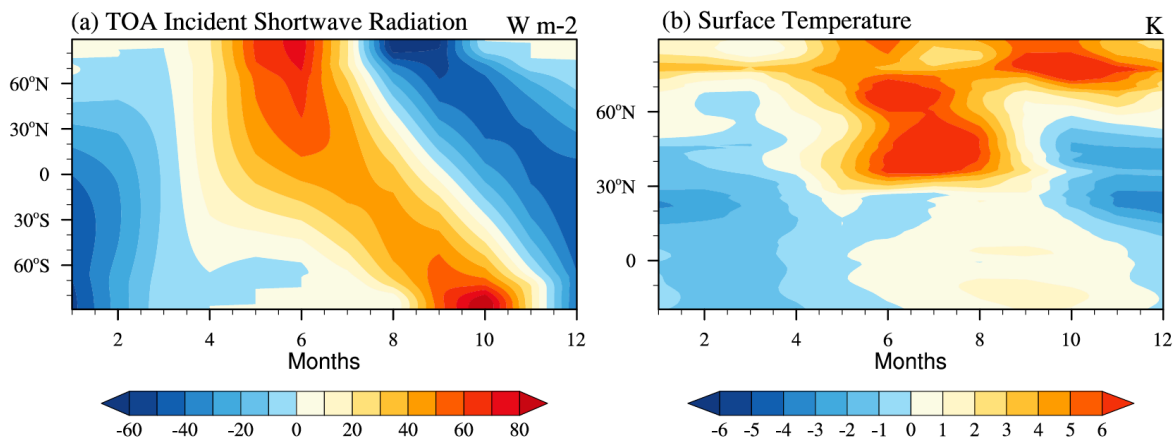
170

171 Figure 1. Proxy time-series of $\delta^{18}\text{O}$ from Bittoo Cave (BT-2.3: black, BT-5: black/orange) and
 172 Mawmluh Cave (MAW-3: blue). Data presented in ‰ relative to VPDB (Vienna Pee Dee
 173 Belemnite) standard. LIG/MIS-5e is shaded in grey.

174 Magiera et al. (2019) also investigated other proxies besides $\delta^{18}\text{O}$. Using a combination of $\delta^{18}\text{O}$,
 175 $\delta^{44}\text{Ca}$, and elemental measurements, the authors concluded that the wettest period was between
 176 135 and 100 ka before present, corresponding to the LIG/MIS-5e. The decrease in oxygen
 177 isotopes found in the speleothem at both Bittoo cave and Mawmluh cave suggests a stronger
 178 ISM with a more remote moisture source than the periods before and after the LIG. Proxy-record
 179 evidence of increased monsoon precipitation has also been found for the East Asian summer
 180 monsoon, suggesting that the two monsoon systems have a coupled response to changes in
 181 orbital forcing (Liu et al., 2020; Scussolini et al., 2019).

182

183 4 Enhanced land–sea contrast due to orbital forcing



184

185 Figure 2. Differences between the LIG and PI periods (LIG minus PI, the same in other figures)
 186 in (a) zonal mean TOA insolation and (b) surface temperature, averaged over 50°E – 100°E .

187 Differences in the Earth's orbital parameters (the perihelion, obliquity, and eccentricity) during
 188 the LIG led to differences in the seasonal and latitudinal distribution of solar radiation received
 189 at the top of the atmosphere (TOA) compared with PI conditions (Berger & Loutre, 1991; Otto-
 190 Bliesner et al., 2017). The incoming solar radiation received by the Northern Hemisphere
 191 (calculated as the zonal mean over 0°N – 90°N) increased by 20.8 W/m^2 from June to September

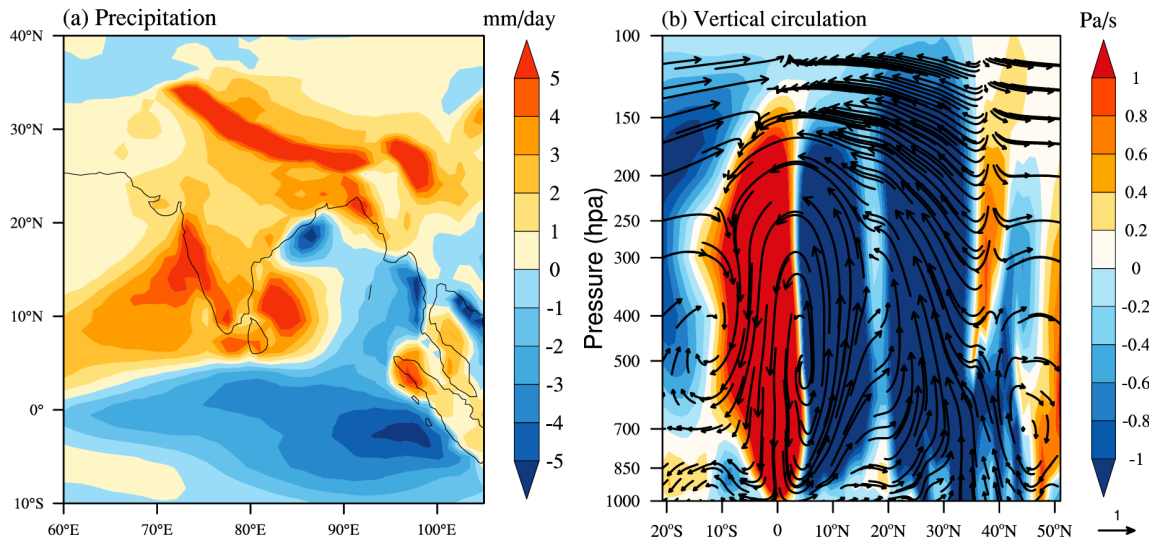
192 (JJAS) during the LIG period, which is 7.1% more than that during the PI period (Fig. 2a). The
193 increase in insolation was larger in the Northern Hemisphere than in the Southern Hemisphere,
194 leading to an even larger hemispheric thermal gradient. This contrasts with the current global
195 warming situation, where the growth rate of atmospheric internal energy in the Southern
196 Hemisphere is higher than in the Northern Hemisphere (Chen et al., 2020).

197 Increased solar radiation at the TOA directly affects the amount of heat reaching the surface and
198 changes the surface energy budget. With increased incoming solar radiation in summer, the
199 warming amplitude over land is larger than that over the ocean and this land–sea contrast triggers
200 the onset of the monsoon. During the LIG, the orbital forcing induced surface warming over both
201 land and ocean, but the warming amplitude was larger over the land than over the ocean (Fig.
202 2b). The surface temperature of West Asia increased by ~ 3.6 °C in JJAS, whereas the surface
203 temperature of the northern Indian Ocean increased by only 0.6°C (Fig. 2b). We calculate the
204 land–sea contrast by taking the temperature difference between the Eurasian continent (10°N–
205 90°N, 50°E–100°E) and the Indian Ocean (30°S–10°N and 50°E–100°E). The land–sea contrast
206 in the PI period was 10.4 °C over the Indian monsoon region, but during the LIG it was ~ 3 °C
207 larger. In other words, the land–sea contrast was enhanced by $\sim 28\%$ during the LIG compared
208 with the PI period.

209 An increase in the land–sea thermal contrast should enhance the monsoon and lead to more
210 monsoon precipitation (Chou, 2003; Wu et al., 2012). Previous studies have shown an increase in
211 precipitation in the Indian subcontinent during the LIG period, indicating an enhanced monsoon
212 (Magiera et al., 2019; Montoya et al., 2000). Here we quantify the differences in the intensity of
213 the ISM between the LIG and PI periods using the DNS method proposed by Li & Zeng (2002).
214 The DNS index indicates that the average intensity of the ISM during the LIG was 38% larger
215 than during the PI period (not shown).

216 In summary, during the LIG, the land–sea thermal contrast was 28% larger than during the PI
217 period and the DNS monsoon index was 38% larger. The enhancement of the monsoon and
218 land–sea contrast resulted directly from the differences in insolation. We show below that other
219 indirect impacts further amplified the land–sea contrast and monsoon intensity.

220

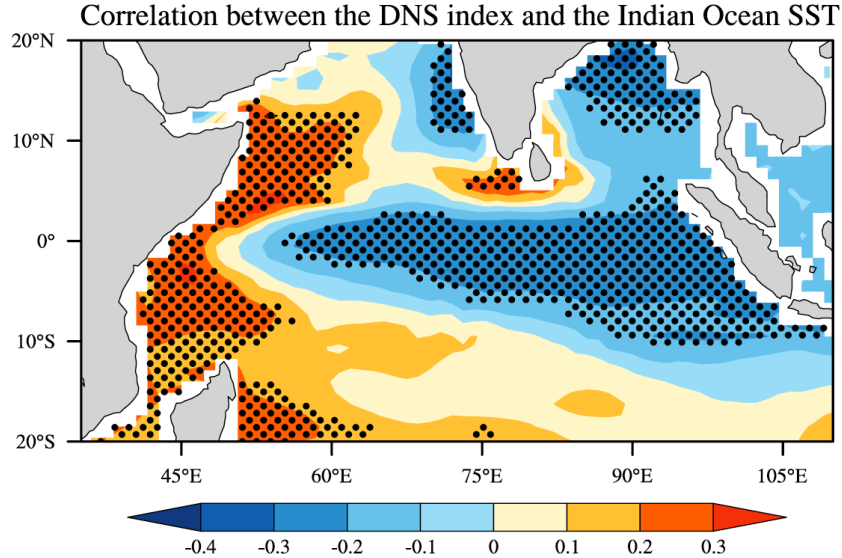
221 **5 Local response to orbital forcing**

222

223 Figure 3. Differences between the LIG and PI periods in (a) precipitation and (b) vertical
 224 circulation averaged over 60°E–100°E.

225 Turner & Annamalai (2012) note that under current GHGs forcing, although the increased land–
 226 sea contrast and water vapor should theoretically exacerbate monsoon precipitation,
 227 observational results do not provide any cogent evidence for such a positive trend, and even
 228 suggest a negative trend. This phenomenon may be related to the complex dynamical feedbacks
 229 within the tropical Indo-Pacific region. In contrast, during the LIG warm period, there was a
 230 significant increase of ~28% in Indian summer monsoon precipitation compared with the PI
 231 period. The major changes in precipitation were prominent in three areas: increased precipitation
 232 on the south side of the Himalayas and on the west side of the Western Ghats, and reduced
 233 precipitation over the equatorial eastern Indian Ocean (Figure 3a).

234 The changes in the vertical circulation (Fig. 3b) correspond well to the changes in Indian
 235 monsoon precipitation (Fig. 3a). Two prominent local Hadley circulations resemble a "Double-
 236 Wall" structure. The ascending air flow near 10°N and 30°N is within the Indian subcontinent
 237 and corresponds to the high precipitation centers shown in Fig. 3a. The descending branch is
 238 located in the equatorial region around 10°S–5°N and corresponds to the reduced precipitation in
 239 the equatorial eastern Indian Ocean. This suggests that the monsoonal flow carried water vapor
 240 northward from the Indian Ocean, resulting in strong convection when the topographic barrier
 241 was reached. The relationship between the precipitation anomaly pattern and the topography
 242 emphasizes the influence of topography and the vertical atmospheric motion on precipitation
 243 (Bookhagen & Burbank, 2006; Sudharsan et al., 2020). External forcing, such as the orbital
 244 forcing during the LIG, could have resulted in an anomalous near-surface cyclone over the
 245 Tibetan Plateau (see Fig. 5a in next section), leading to anomalous upward flow. This might have
 246 strengthened the ISM and been conducive to the transport of water vapor from the Bay of Bengal
 247 and the Arabian Sea to the Indian subcontinent. The external forcing might also have further
 248 amplified the "pumping" effect over the Tibetan Plateau in summer (Wu et al., 2015).

249 **6 Ocean feedbacks and remote forcing from the Pacific**

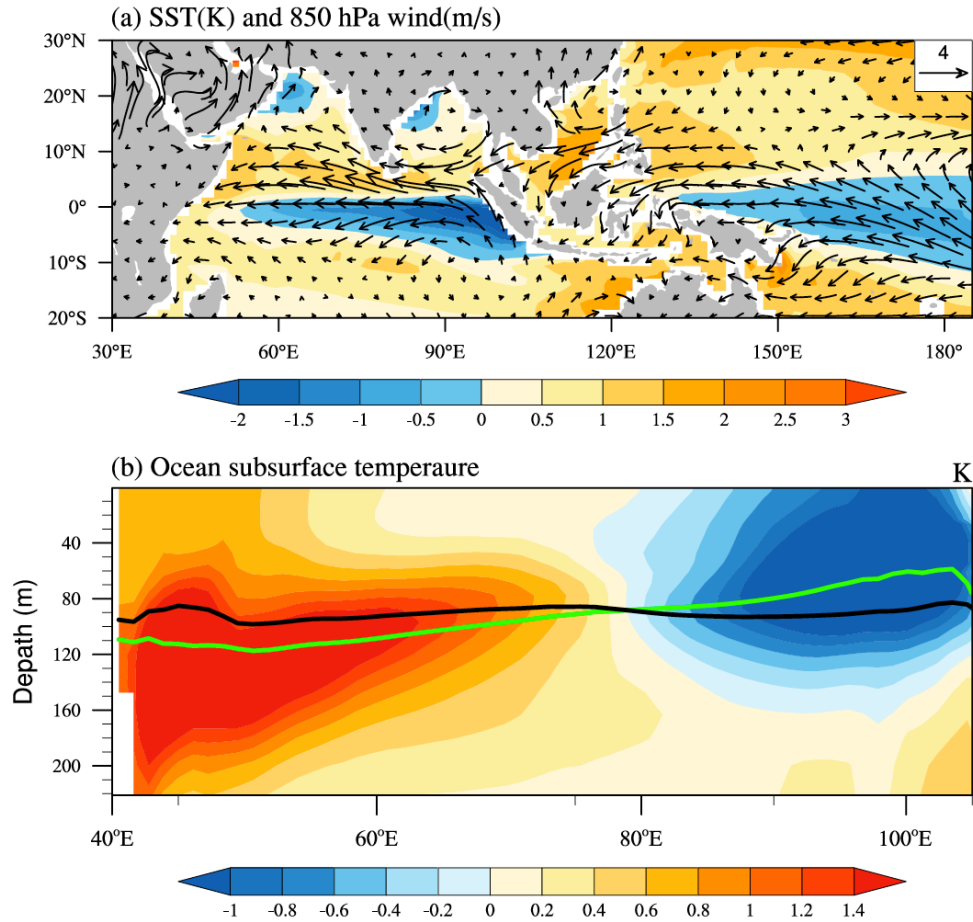
250

251 Figure 4. Correlation between the DNS index and the Indian Ocean SST in JJAS during the LIG
 252 period. The correlation is calculated using 100 years of data from the EC-Earth3-LR LIG
 253 simulation. The stippled area indicates statistical significance at the 0.05 level.

254

255 Saji et al. (1999) showed that the tropical Indian Ocean SST has an important influence on the
 256 Indian summer monsoon. Figure 4 shows the correlation between the intensity of the Indian
 257 summer monsoon (as measured by the DNS index) and the tropical Indian Ocean SST in the LIG
 258 period. The conventional monsoon index based on precipitation is primarily statistical, whereas
 259 the DNS method, by taking the wind field into account, is more strongly grounded in
 260 atmospheric dynamics and describes regional circulations more clearly and accurately (Li et al.,
 261 2010; Zhang et al., 2018). Figure 4 shows that there was a statistically significant correlation
 262 between the equatorial Indian Ocean SST and the DNS index during the LIG. The correlation
 263 exhibits a dipole pattern, with negative correlations in the eastern part of the equatorial Indian
 264 Ocean and positive correlations in the western part.

265 This correlation pattern resembles the SST differences between the LIG and PI periods (Fig. 5a).
 266 During the LIG, there was a cold tongue in the eastern equatorial Indian Ocean, with the largest
 267 part lying in the Southern Hemisphere. The increased insolation during the LIG (Fig. 2a) did not
 268 prevent the formation of this cold tongue and the strong seasonal hemispheric thermal contrast.
 269 The cooling might have been associated with the enhancement of the Indian summer monsoon,
 270 as shown in Fig. 5a. Bollasina & Ming (2013) showed that the spatial expansion of the Indian
 271 Ocean SST mode can affect ocean convection through the modulation of the atmospheric
 272 meridional circulation. Such an SST pattern increased the meridional SST gradient in the
 273 equatorial Indian Ocean during the LIG. The air on the west side was warmed and rose up
 274 whereas on the east side it was cooled and sunk down, thus strengthening the anomalous easterly
 275 winds at the surface of the equatorial Indian Ocean.



276

277 Figure 5. Differences between the LIG and PI periods in (a) 850 hPa wind (vectors), sea surface
 278 temperature (shading), and (b) ocean subsurface temperature, averaged over 10°S–5°N. The
 279 green line in (b) indicates the thermocline (represented by 23°C isotherm) during the LIG, and
 280 the black line indicates the thermocline in the PI period.

281 Furthermore, the Pacific Ocean can establish a connection with the tropical Indian Ocean
 282 through atmospheric circulation (Terray et al., 2021; Tokinaga et al., 2012), which can contribute
 283 to the generation of anomalous easterly winds. In addition to the hemispheric thermal contrast in
 284 the Indian Ocean in JJAS, there was a strong SST gradient between the northern and southern
 285 Pacific Ocean (Fig. 5a). As the SST increased in the North Pacific, the air mass warmed and
 286 sunk over the cold SST in the South Pacific, creating a meridional Hadley Circulation over the
 287 Pacific Ocean (not shown). Due to the leftward geostrophic deflection in the Southern
 288 Hemisphere, the downdrafts were deflected westward over the sea surface, forming anomalous
 289 easterly winds over the equatorial western Pacific and Indo-Pacific Warm Pool. According to
 290 ocean–atmosphere coupling theory (Bjerknes, 1969), the upwelling of the equatorial eastern
 291 Indian Ocean was enhanced under the action of the anomalous easterly winds. As the
 292 thermocline became shallower (deeper) in the equatorial eastern (western) Indian Ocean, the SST
 293 formed a dipole corresponding to the "warm West and cold East" pattern (Figure 5b). In addition,
 294 with the expansion of the SST cooling area in the equatorial eastern Indian Ocean, the land–sea
 295 thermal gradient in South Asia was further increased, which had a positive feedback effect on the
 296 Indian summer monsoon precipitation.

297 **7 Conclusions**

298 Based on the EC-Earth3-LR model, this work explored whether the LIG could act as a potential
299 analogue of the Indian monsoon system under global warming. Warming in the LIG was caused
300 by different external forcing to current global warming; GHGs are the main external forcing of
301 current warming, whereas orbital forcing drove the hemispheric thermal contrast during the LIG.
302 We found that the Indian summer monsoon was intensified by the orbital forcing during the LIG,
303 which is in contrast to the weakening of the monsoon that has occurred under GHGs forcing. We
304 discussed the physical mechanisms behind the enhanced Indian summer monsoon from two
305 perspectives: the direct effect of the land–sea contrast and the further amplification through
306 ocean feedbacks.

307 The direct effect of orbital forcing during the LIG enhanced the land–sea contrast in the Indian
308 monsoon region by imposing a stronger hemispheric thermal gradient. The enhanced monsoon
309 flow facilitated the “pumping effect” around the Tibetan Plateau and brought more water vapor
310 from the Indian Ocean to the Indian subcontinent. Meanwhile, two anomalous meridional Hadley
311 circulation structures were formed through topographic uplift, leading to increased precipitation
312 on the coast of the Western Ghats and on the south side of the Himalayas, and a significant
313 decrease in precipitation in the equatorial eastern Indian Ocean. Furthermore, the hemispheric
314 thermal contrast formed anomalous easterly winds in the equatorial eastern Indian Ocean. A
315 similar mechanism in the western Pacific resulted in anomalous easterly winds, which further
316 enhanced the easterly winds in the eastern Indian Ocean. The weakened westerly winds led to a
317 shallower thermocline in the equatorial eastern Indian Ocean and the subsequent upwelling
318 enlarged the cooling area of the sea surface. A cooler eastern Indian Ocean further increased the
319 thermal gradient between the Eurasian continent and the northern Indian Ocean, thus enhancing
320 the Indian summer monsoon. The results indicate that during the LIG, the different insolation
321 from today caused by orbital forcing enhanced the Indian summer monsoon, and this effect was
322 further amplified by the ocean feedbacks in the eastern Indian Ocean and the western Pacific.

323 In summary, unlike the weakening of the monsoon caused by GHGs warming, the warming
324 during the LIG enhanced the interhemispheric thermal gradient, which strengthened the Indian
325 summer monsoon. This mechanism is specific to the Indian monsoon, where the land–sea
326 contrast is in the north–south direction. The hemispheric thermal contrast may not affect the
327 West African monsoon or the East Asian monsoon, where the land–sea contrast is in the west–
328 east direction. We expect that the mechanisms behind the response of the Indian summer
329 monsoon to orbital forcing during the LIG revealed in this paper will be of substantial and
330 practical value for understanding past climate variability in South Asia and for interpreting future
331 climate change.

332

333 **Acknowledgements and Data Availability Statement**

334 This work was supported by the Swedish Research Council (Vetenskapsrådet, grant no. 2013-
335 06476 and 2017-04232) and National Natural Science Foundation of China (NSFC) Project
336 (41790474, 41530424) and Shandong Natural Science Foundation Project (ZR2019ZD12), and
337 the Fundamental Research Funds for the Central Universities (201962009). The EC-Earth
338 simulations were performed on ECMWF's computing and archive facilities. Additional resources
339 were provided by the Swedish National Infrastructure for Computing (SNIC) at the National
340 Supercomputer Centre (NSC) partially funded by the Swedish Research Council through grant

341 agreement no. 2018-05913. The model simulation data are available at the website <https://esgf->
342 [data.dkrz.de/search/cmip6-dkrz](https://esgf-data.dkrz.de/search/cmip6-dkrz).

343 The model simulations analysed in this study are distributed and made freely available through
344 the Earth System Grid Federation (ESGF). The PI simulations are available at
345 <https://doi.org/10.22033/ESGF/CMIP6.4847> (EC-Earth Consortium (EC-Earth), 2019). The LIG
346 simulations are available at <https://doi.org/10.22033/ESGF/CMIP6.4798> (EC-Earth Consortium
347 (EC-Earth), 2020).

348 Details on the ESGF can be found on the website of the CMIP panel (<https://www.wcrp->
349 [climate.org/wgcm-cmip/wgcm-cmip6](https://www.wcrp-climate.org/wgcm-cmip/wgcm-cmip6)). The reconstruction data used for data–model comparison
350 is in the Supplement.

351

352 **References**

353 Balsamo, G., Viterbo, P., Beljaars, A., van den Hurk, B., Hirschi, M., Betts, A. K., & Scipal, K.
354 (2009). A revised hydrology for the ECMWF model: Verification from field site to
355 terrestrial water storage and impact in the Integrated Forecast System. *Journal of*
356 *Hydrometeorology*, *10*(3), 623. <https://doi.org/10.1175/2008JHM1068.1>

357 Berger, A., & Loutre, M.-F. (1991). Insolation values for the climate of the last 10 million years.
358 *Quaternary Science Reviews*, *10*(4), 297-317. [https://doi.org/10.1016/0277-3791\(91\)90033-](https://doi.org/10.1016/0277-3791(91)90033-Q)
359 [Q](https://doi.org/10.1016/0277-3791(91)90033-Q)

360 Bjerknes, J. (1969). Atmospheric teleconnections from the equatorial Pacific. *Monthly Weather*
361 *Review*, *97*(3), 163-172. [https://doi.org/10.1175/1520-0493\(1969\)0972.3.CO;2](https://doi.org/10.1175/1520-0493(1969)0972.3.CO;2)

362 Bollasina, M. A., & Ming, Y. (2013). The general circulation model precipitation bias over the
363 southwestern equatorial Indian Ocean and its implications for simulating the South Asian
364 monsoon. *Climate dynamics*, *40*(3), 823-838. <https://doi.org/10.1007/s00382-012-1347-7>

365 Bookhagen, B., & Burbank, D. W. (2006). Topography, relief, and TRMM - derived rainfall
366 variations along the Himalaya. *Geophysical Research Letters*, *33*(8), 153-172.
367 <https://doi.org/10.1029/2006GL026944>

368 Buckley, B. M., Fletcher, R., Wang, S.-Y. S., Zottoli, B., & Pottier, C. (2014). Monsoon
369 extremes and society over the past millennium on mainland Southeast Asia. *Quaternary*
370 *Science Reviews*, *95*(7), 1-19. <https://doi.org/10.1016/j.quascirev.2014.04.022>

371 Cai, Y., Fung, I. Y., Edwards, R. L., An, Z., Cheng, H., Lee, J.-E., et al. (2015). Variability of
372 stalagmite-inferred Indian monsoon precipitation over the past 252,000 y. *Proceedings of*
373 *the National Academy of Sciences*, *112*(10), 2954-2959.
374 <https://doi.org/10.1073/pnas.1424035112>

375 Chen, K., Li, J., Xie, T., Wang, Q., & Wang, L. 2020. Analysis of the Spatiotemporal
376 Characteristics and Trends of Global Atmospheric Energy. *Chinese Journal of Atmospheric*
377 *Sciences (in Chinese)*, *44*(1): 168-182. <https://doi.org/10.3878/j.issn.1006-9895.1903.18252>

378 Cheng, H., Edwards, R. L., Sinha, A., Spötl, C., Yi, L., Chen, S., et al. (2016). The Asian
379 monsoon over the past 640,000 years and ice age terminations. *Nature*, *534*(7609), 640-646.
380 <https://doi.org/10.1038/nature18591>

- 381 Chou, C. (2003). Land–sea heating contrast in an idealized Asian summer monsoon. *Climate*
382 *Dynamics*, 21(1), 11-25. <https://doi.org/10.1007/s00382-003-0315-7>
- 383 Craig, A., Valcke, S., & Coquart, L. (2017). Development and performance of a new version of
384 the OASIS coupler, OASIS3-MCT_3.0. *Geoscientific Model Development*, 10(9), 3297-
385 3308. <https://doi.org/10.5194/gmd-2017-64>
- 386 Dinezio, P. N., Puy, M., Thirumalai, K., Jin, F.-F., & Tierney, J. E. (2020). Emergence of an
387 equatorial mode of climate variability in the Indian Ocean. *Science Advances*, 6(19),
388 eaay7684. <https://doi.org/10.1126/sciadv.aay7684>
- 389 EC-Earth Consortium (EC-Earth). (2019). EC-Earth-Consortium ECEarth3-LR model output
390 prepared for CMIP6 CMIP piControl, Version 20200409. *Earth System Grid Federation*.
391 <https://doi.org/10.22033/ESGF/CMIP6.4847>
- 392 EC-Earth Consortium (EC-Earth). (2020). EC-Earth-Consortium ECEarth3-LR model output
393 prepared for CMIP6 PMIP lig127k, Version 20200409. *Earth System Grid Federation*.
394 <https://doi.org/10.22033/ESGF/CMIP6.4798>, 2020.
- 395 Gadgil, S., & Kumar, K. R. (2006). The Asian monsoon-agriculture and economy. In *The Asian*
396 *Monsoon* (pp. 651–683). Berlin, Heidelberg: Springer.
- 397 Goswami, B. N., Venugopal, V., Sengupta, D., Madhusoodanan, M., & Xavier, P. K. (2006).
398 Increasing trend of extreme rain events over India in a warming environment. *Science*,
399 314(5804), 1442-1445. <https://doi.org/1442-1445>. 10.1126/science.1132027
- 400 Han, Z., Su, T., Zhang, Q., Wen, Q., & Feng, G. (2019). Thermodynamic and dynamic effects of
401 increased moisture sources over the Tropical Indian Ocean in recent decades. *Climate*
402 *Dynamics*, 53(11), 7081–7096. <https://doi.org/7081-7096>. 10.1007/s00382-019-04977-w
- 403 Harrison, S. P., Bartlein, P., Izumi, K., Li, G., Annan, J., Hargreaves, J., et al. (2015). Evaluation
404 of CMIP5 palaeo-simulations to improve climate projections. *Nature Climate Change*, 5(8),
405 735-743. <https://doi.org/10.1038/nclimate2649>
- 406 Hazeleger, W., Severijns, C., Semmler, T., Stefanescu, S., Yang, S., Wang, X., et al. (2010). EC-
407 earth: a seamless earth-system prediction approach in action. *Bulletin of the American*
408 *Meteorological Society*, 91(10), 1357-1363. <https://doi.org/10.1175/2010BAMS2877.1>
- 409 Hazeleger, W., Wang, X., Severijns, C., Ștefănescu, S., Bintanja, R., Sterl, A., et al. (2012). EC-
410 Earth V2. 2: description and validation of a new seamless earth system prediction model.
411 *Climate Dynamics*, 39(11), 2611-2629. <https://doi.org/10.1007/s00382-011-1228-5>
- 412 Hirabayashi, Y., Mahendran, R., Koirala, S., Konoshima, L., Yamazaki, D., Watanabe, S., et al.
413 (2013). Global flood risk under climate change. *Nature Climate Change*, 3(9), 816-821.
414 <https://doi.org/10.1038/NCLIMATE1911>
- 415 Hoffman, J. S., Clark, P. U., Parnell, A. C., & He, F. (2017). Regional and global sea-surface
416 temperatures during the last interglaciation. *Science*, 355(6322), 276-279.
417 <https://doi.org/10.1126/science.aai8464>
- 418 Kageyama, M., Braconnot, P., Harrison, S. P., Haywood, A. M., Jungclaus, J. H., Otto-Bliesner,
419 B. L., et al. (2018). The PMIP4 contribution to CMIP6–Part 1: Overview and over-arching
420 analysis plan. *Geoscientific Model Development*, 11(3), 1033-1057.
421 <https://doi.org/10.5194/gmd-11-1033-2018>

- 422 Kathayat, G., Cheng, H., Sinha, A., Spötl, C., Edwards, R. L., Zhang, H., et al. (2016). Indian
423 monsoon variability on millennial-orbital timescales. *Scientific Reports*, 6(1), 1-7.
424 <https://doi.org/10.1038/srep24374>
- 425 Kitoh, A., Endo, H., Krishna Kumar, K., Cavalcanti, I. F., Goswami, P., & Zhou, T. (2013).
426 Monsoons in a changing world: A regional perspective in a global context. *Journal of*
427 *Geophysical Research: Atmospheres*, 118(8), 3053-3065.
428 <https://doi.org/10.1002/jgrd.50258>
- 429 Lechleitner, F. A., Breitenbach, S. F., Rehfeld, K., Ridley, H. E., Asmerom, Y., Pruffer, K. M., et
430 al. (2017). Tropical rainfall over the last two millennia: evidence for a low-latitude
431 hydrologic seesaw. *Scientific Reports*, 7(1), 1-9. <https://doi.org/10.1038/srep45809>
- 432 Li, J., & Zeng, Q. (2000). Significance of the normalized seasonality of wind field and its
433 rationality for characterizing the monsoon. *Science in China Series D: Earth Sciences*,
434 43(6), 646-653. <https://doi.org/10.1007/BF02879509>
- 435 Li, J., & Zeng, Q. (2002). A unified monsoon index. *Geophysical Research Letters*, 29(8), 1274.
436 [10.1029/2001GL013874](https://doi.org/10.1029/2001GL013874)
- 437 Li, J., Wu, Z., Jiang, Z., & He, J. (2010). Can global warming strengthen the East Asian summer
438 monsoon? *Journal of Climate*, 23(24), 6696-6705. <https://doi.org/10.1175/2010JCLI3434.1>
- 439 Li, T. (2018). False amount effect—a discussion on one issue of isotopic climatology.
440 *Quaternary Sciences*, 38(6), 1545-1548. [https://doi.org/10.11928/j.issn.1001-](https://doi.org/10.11928/j.issn.1001-7410.2018.06.20)
441 [7410.2018.06.20](https://doi.org/10.11928/j.issn.1001-7410.2018.06.20)
- 442 Liu, G., Li, X., Chiang, H.-W., Cheng, H., Yuan, S., Chawchai, S., et al. (2020). On the glacial-
443 interglacial variability of the Asian monsoon in speleothem $\delta^{18}\text{O}$ records. *Science Advances*,
444 6(7), eaay8189. <https://doi.org/10.1126/sciadv.aay8189>
- 445 Lunt, D. J., Abe-Ouchi, A., Bakker, P., Berger, A., Braconnot, P., Charbit, S., et al. (2013). A
446 multi-model assessment of last interglacial temperatures. *Climate of the Past*, 9(2), 699-717.
447 <https://doi.org/10.5194/cp-9-699-2013>
- 448 Madec, G. (2008). NEMO reference manual, ocean dynamic component: NEMO-OPA. In *Note*
449 *du Pôle modélisation, Inst. Pierre Simon Laplace, Fr.* (Tech. Rep., 27).
- 450 Magiera, M., Lechleitner, F. A., Erhardt, A. M., Hartland, A., Kwiciecien, O., Cheng, H., et al.
451 (2019). Local and regional Indian Summer Monsoon precipitation dynamics during
452 Termination II and the Last Interglacial. *Geophysical Research Letters*, 46(21), 12454-
453 12463. <https://doi.org/10.1029/2019GL083721>
- 454 Midhun, M., Lekshmy, P., Ramesh, R., Yoshimura, K., Sandeep, K., Kumar, S., et al. (2018).
455 The effect of monsoon circulation on the stable isotopic composition of rainfall. *Journal of*
456 *Geophysical Research: Atmospheres*, 123(10), 5205-5221.
457 <https://doi.org/10.1029/2017JD027427>
- 458 Montoya, M., von Storch, H., & Crowley, T. J. (2000). Climate simulation for 125 kyr BP with a
459 coupled ocean-atmosphere general circulation model. *Journal of Climate*, 13(6), 1057-
460 1072. [https://doi.org/10.1175/1520-0442\(2000\)0132.0.CO;2](https://doi.org/10.1175/1520-0442(2000)0132.0.CO;2)

- 461 Nikolova, I., Yin, Q., Berger, A., Singh, U. K., & Karami, M. P. (2013). The last interglacial
462 (Eemian) climate simulated by LOVECLIM and CCSM3. *Climate of the Past*, 9(4), 1789-
463 1806. <https://doi.org/10.5194/cpd-8-5293-2012>
- 464 Otto-Bliesner, B. L., Braconnot, P., Harrison, S. P., Lunt, D. J., Abe-Ouchi, A., Albani, S., et al.
465 (2017). The PMIP4 contribution to CMIP6–Part 2: Two interglacials, scientific objective
466 and experimental design for Holocene and Last Interglacial simulations. *Geoscientific*
467 *Model Development*, 10(11), 3979-4003. <https://doi.org/10.5194/gmd-2016-279>
- 468 Pedersen, R. A., Langen, P. L., & Vinther, B. M. (2017). The last interglacial climate: comparing
469 direct and indirect impacts of insolation changes. *Climate Dynamics*, 48(9), 3391-3407.
470 <https://doi.org/10.1007/s00382-016-3274-5>
- 471 Ramesh, K., & Goswami, P. (2007). Reduction in temporal and spatial extent of the Indian
472 summer monsoon. *Geophysical Research Letters*, 34(23).
473 <https://doi.org/10.1029/2007GL031613>
- 474 Roxy, M. K., Ritika, K., Terray, P., Murtugudde, R., Ashok, K., & Goswami, B. (2015). Drying
475 of Indian subcontinent by rapid Indian Ocean warming and a weakening land-sea thermal
476 gradient. *Nature communications*, 6(1), 1-10. <https://doi.org/10.1038/ncomms8423>
- 477 Saha, A., Ghosh, S., Sahana, A.S., et al. (2014). Failure of CMIP5 climate models in simulating
478 post-1950 decreasing trend of Indian monsoon. *Geophysical Research Letters*, 41(20):
479 7323-7330. <https://doi.org/10.1002/2014GL061573>
- 480 Saji, N., Goswami, B., Vinayachandran, P., & Yamagata, T. (1999). A dipole mode in the
481 tropical Indian Ocean. *Nature*, 401(6751), 360-363. <https://doi.org/10.1038/43854>
- 482 Scussolini, P., Bakker, P., Guo, C., Stepanek, C., Zhang, Q., Braconnot, P., et al. (2019).
483 Agreement between reconstructed and modeled boreal precipitation of the Last Interglacial.
484 *Science Advances*, 5(11), eaax7047. <https://doi.org/10.1126/sciadv.aax7047>
- 485 Singh, D., Tsiang, M., Rajaratnam, B., & Diffenbaugh, N. S. (2014). Observed changes in
486 extreme wet and dry spells during the South Asian summer monsoon season. *Nature*
487 *Climate Change*, 4(6), 456-461. <https://doi.org/10.1038/nclimate2208>
- 488 Sinha, A., Kathayat, G., Cheng, H., Breitenbach, S. F., Berkelhammer, M., Mudelsee, M., et al.
489 (2015). Trends and oscillations in the Indian summer monsoon rainfall over the last two
490 millennia. *Nature Communications*, 6(1), 1-8. <https://doi.org/10.1038/ncomms7309>
- 491 Sudharsan, N., Karmakar, S., Fowler, H. J., & Hari, V. (2020). Large-scale dynamics have
492 greater role than thermodynamics in driving precipitation extremes over India. *Climate*
493 *Dynamics*, 55(9), 2603-2614. <https://doi.org/10.1007/s00382-020-05410-3>
- 494 Tan, M. (2014). Circulation effect: response of precipitation $\delta^{18}\text{O}$ to the ENSO cycle in monsoon
495 regions of China. *Climate Dynamics*, 42(3-4), 1067-1077. [10.1007/s00382-013-1732-x](https://doi.org/10.1007/s00382-013-1732-x)
- 496 Terray, P., Sooraj, K., Masson, S., & Prodhomme, C. (2021). Anatomy of the Indian Summer
497 Monsoon and ENSO relationships in state-of-the-art CGCMs: Role of the tropical Indian
498 Ocean. *Climate Dynamics*, 56(1), 329-356. <https://doi.org/10.1007/s00382-020-05484-z>
- 499 Tokinaga, H., Xie, S.-P., Deser, C., Kosaka, Y., & Okumura, Y. M. (2012). Slowdown of the
500 Walker circulation driven by tropical Indo-Pacific warming. *Nature*, 491(7424), 439-443.
501 <https://doi.org/10.1038/nature11576>

- 502 Turner, A. G., & Annamalai, H. (2012). Climate change and the South Asian summer monsoon.
503 *Nature Climate Change*, 2(8), 587-595. <https://doi.org/10.1038/nclimate1495>
- 504 Turney, C. S., & Jones, R. T. (2010). Does the Agulhas Current amplify global temperatures
505 during super-interglacials? *Journal of Quaternary Science*, 25(6), 839-843.
506 <https://doi.org/10.1002/jqs.1423>
- 507 Turney, C. S., Jones, R. T., McKay, N. P., Van Sebille, E., Thomas, Z. A., Hillenbrand, C.-D., &
508 Fogwill, C. J. (2020). A global mean sea surface temperature dataset for the Last
509 Interglacial (129–116 ka) and contribution of thermal expansion to sea level change. *Earth*
510 *System Science Data*, 12(4), 3341-3356. <https://doi.org/10.5194/essd-12-3341-2020>
- 511 Vancoppenolle, M., Bouillon, S., Fichet, T., Goosse, H., Lecomte, O., Morales Maqueda, M.,
512 & Madec, G. (2012). The Louvain-la-Neuve sea ice model. *Notes du pôle de modélisation*,
513 *Institut Pierre-Simon Laplace (IPSL)*. Paris, France.
- 514 Vittal, H., Karmakar, S., Ghosh, S., & Murtugudde, R. (2020). A comprehensive India-wide
515 social vulnerability analysis: highlighting its influence on hydro-climatic risk.
516 *Environmental Research Letters*, 15(1), 014005. <https://doi.org/10.1088/1748-9326/ab6499>
- 517 Wang, B., Wu, Z., Li, J., Liu, J., Chang, C.-P., Ding, Y., & Wu, G. (2008). How to measure the
518 strength of the East Asian summer monsoon. *Journal of Climate*, 21(17), 4449-4463.
519 <https://doi.org/10.1175/2008JCLI2183.1>
- 520 Wang, Y., Cheng, H., Edwards, R. L., Kong, X., Shao, X., Chen, S., et al. (2008). Millennial-and
521 orbital-scale changes in the East Asian monsoon over the past 224,000 years. *Nature*,
522 451(7182), 1090-1093. <https://doi.org/10.1038/nature06692>
- 523 Wu, G., Duan, A., Liu, Y., Mao, J., Ren, R., Bao, Q., et al. (2015). Tibetan Plateau climate
524 dynamics: recent research progress and outlook. *National Science Review*, 2(1), 100-116.
525 <https://doi.org/10.1093/nsr/nwu045>
- 526 Wu, G., Liu, Y., He, B., Bao, Q., Duan, A., & Jin, F.-F. (2012). Thermal controls on the Asian
527 summer monsoon. *Scientific Reports*, 2(1), 1-7. <https://doi.org/10.1038/srep00404>
- 528 Zhang, Q., Berntell, E., Axelsson, J., Chen, J., Han, Z., de Nooijer, W., et al. (2021). Simulating
529 the mid-Holocene, last interglacial and mid-Pliocene climate with EC-Earth3-LR.
530 *Geoscientific Model Development*, 14(2), 1147-1169. [https://doi.org/10.5194/gmd-14-1147-](https://doi.org/10.5194/gmd-14-1147-2021)
531 2021
- 532 Zhang, Y., Li, J., Xue, J., Feng, J., Wang, Q., Xu, Y., et al. (2018). Impact of the South China
533 Sea summer monsoon on the Indian Ocean dipole. *Journal of Climate*, 31(16), 6557-6573.
534 <https://doi.org/10.1175/JCLI-D-17-0815.1>
- 535